Research Article | Vol. 26, No. 9 | 30 Apr 2018 | OPTICS EXPRESS 12318

Optics EXPRESS

Numerical investigation of nematic liquid crystals in the THz band based on EIT sensor

PENG-YUAN WANG,[1] TAO JIN,[2] FAN-YI MENG,[3,*] YUE-LONG LYU,[3] DANIEL ERNI,[4] QUN WU,[1,3] AND LEI ZHU[5]

[1]*Department of Electronic Science and Technology, Harbin Institute of Technology, Harbin 150001, China*
[2]*Department of Electronic Information Engineering, School of Information and Electrical Engineering, Harbin Institute of Technology, Weihai 264209, China*
[3]*Department of Microwave Engineering, Harbin Institute of Technology, Harbin 150001, China*
[4]*Laboratory for General and Theoretical Electrical Engineering (ATE), Faculty of Engineering, University of Duisburg-Essen, D-47048 Duisburg, Germany*
[5]*Communication and Electronics Engineering Institute, Qiqihar University, Qiqihar 161006, China*
**blade@hit.edu.cn*

Abstract: This paper introduces the concept of electromagnetically induced transparency (EIT) into the permittivity extraction of an anisotropic material—nematic liquid crystal (NLC). A novel two-step strategy is presented to extract the complex permittivity of the NLC at the THz band, which evaluates the relative permittivity tensor from the resonant frequencies and then determines the loss tangent from the quality factor Q of the EIT sensor. The proposed method features high accuracy due to the sharp resonance of the EIT sensor and also high robustness to the thickness of the NLC layer because only amplitude rather than phase information of the transmission coefficients is required. The NLC filled EIT sensor shows a sensitivity of 56.8 μm/RIU (the resonance wavelength shift over the refractive index change unit (RIU)) and Figure of Merit (FoM) of 6.92. The uncertainty of the proposed technique in the relative permittivity and loss tangent is 3% and 8.2%, respectively.

OCIS codes: (160.3710) Liquid crystals; (130.6010) Sensors; (160.1190) Anisotropic optical materials; (300.6495) Spectroscopy, terahertz.

References and links

1. F. Goelden, A. Gaebler, M. Goebel, A. Manabe, S. Mueller, and R. Jakoby, "Tunable liquid crystal phase shifter for microwave frequencies," Electron. Lett. **45**(13), 686–687 (2009).
2. A. L. Franc, O. H. Karabey, G. Rehder, E. Pistono, R. Jakoby, and P. Ferrari, "Compact and Broadband Millimeter-Wave Electrically Tunable Phase Shifter Combining Slow-Wave Effect With Liquid Crystal Technology," IEEE Trans. Microw. Theory Tech. **61**(11), 3905–3915 (2013).
3. C. Weickhmann, N. Nathrath, R. Gehring, A. Gaebler, M. Jost, and R. Jakoby, "Recent measurements of compact electronically tunable liquid crystal phase shifter in rectangular waveguide topology," Electron. Lett. **49**(21), 1345–1347 (2013).
4. G. Perez-Palomino, M. Barba, J. A. Encinar, R. Cahill, R. Dickie, P. Baine, and M. Bain, "Design and Demonstration of an Electronically Scanned Reflectarray Antenna at 100 GHz Using Multiresonant Cells Based on Liquid Crystals," IEEE Trans. Antenn. Propag. **63**(8), 3722–3727 (2015).
5. G. Perez-Palomino, P. Baine, R. Dickie, M. Bain, J. A. Encinar, R. Cahill, M. Barba, and G. Toso, "Design and Experimental Validation of Liquid Crystal-Based Reconfigurable Reflectarray Elements With Improved Bandwidth in F-Band," IEEE Trans. Antenn. Propag. **61**(4), 1704–1713 (2013).
6. W. Hu, R. Cahill, J. A. Encinar, R. Dickie, H. Gamble, V. Fusco, and N. Grant, "Design and Measurement of Reconfigurable Millimeter Wave Reflectarray Cells With Nematic Liquid Crystal," IEEE Trans. Antenn. Propag. **56**(10), 3112–3117 (2008).
7. S. Bildik, S. Dieter, C. Fritzsch, W. Menzel, and R. Jakoby, "Reconfigurable Folded Reflectarray Antenna Based Upon Liquid Crystal Technology," IEEE Trans. Antenn. Propag. **63**(1), 122–132 (2015).
8. S. Ma, G. H. Yang, D. Erni, F. Y. Meng, L. Zhu, Q. Wu, and J. H. Fu, "Liquid Crystal Leaky-Wave Antennas With Dispersion Sensitivity Enhancement," IEEE Trans. Compon. Packaging Manuf. Technol. **7**(5), 792–801 (2017).

#326154 https://doi.org/10.1364/OE.26.012318
Journal © 2018 Received 15 Mar 2018; revised 20 Apr 2018; accepted 24 Apr 2018; published 27 Apr 2018

Optics EXPRESS

9. B. J. Che, T. Jin, D. Erni, F. Y. Meng, Y. L. Lyu, and Q. Wu, "Electrically Controllable Composite Right/Left-Handed Leaky-Wave Antenna Using Liquid Crystals in PCB Technology," IEEE Trans. Compon. Packaging Manuf. Technol. **7**(8), 1331–1342 (2017).
10. W. Hu, R. Dickie, R. Cahill, H. Gamble, Y. Ismail, V. Fusco, D. Linton, N. Grant, and S. Rea, "Liquid Crystal Tunable mm Wave Frequency Selective Surface," IEEE Microw. Wirel. Compon. Lett. **17**(9), 667–669 (2007).
11. A. Ebrahimi, P. Yaghmaee, W. Withayachumnankul, C. Fumeaux, S. Al-Sarawi, and D. Abbott, "Interlayer tuning of X-band frequency-selective surface using liquid crystal," in *2013 Asia-Pacific Microwave Conference Proceedings* (IEEE, 2013), pp. 1118–1120.
12. S. Bulja, D. Mirshekar-Syahkal, R. James, S. E. Day, and F. A. Fernandez, "Measurement of Dielectric Properties of Nematic Liquid Crystals at Millimeter Wavelength," IEEE Trans. Microw. Theory Tech. **58**(12), 3493–3501 (2010).
13. O. Trushkevych, H. Xu, T. Lu, J. A. Zeitler, R. Rungsawang, F. Gölden, N. Collings, and W. A. Crossland, "Broad spectrum measurement of the birefringence of an isothiocyanate based liquid crystal," Appl. Opt. **49**(28), 5212–5216 (2010).
14. O. H. Karabey, *Electronic Beam Steering and Polarization Agile Planar Antennas in Liquid Crystal Technology: Chap. I* (Springer, 2014).
15. L. Wang, S. Ge, W. Hu, M. Nakajima, and Y. Lu, "Graphene-assisted high-efficiency liquid crystal tunable terahertz metamaterial absorber," Opt. Express **25**(20), 23873–23879 (2017).
16. D. C. Zografopoulos, K. P. Prokopidis, R. Dąbrowski, and R. Beccherelli, "Time-domain modeling of dispersive and lossy liquid-crystals for terahertz applications," Opt. Mater. Express **4**(3), 449–457 (2014).
17. K. P. Prokopidis and D. C. Zografopoulos, "Time-domain numerical scheme based on low-order partial-fraction models for the broadband study of frequency-dispersive liquid crystals," J. Opt. Soc. Am. B **33**(4), 622–629 (2016).
18. S. Mueller, A. Penirschke, C. Damm, P. Scheele, M. Wittek, C. Weil, and R. Jakoby, "Broad-band microwave characterization of liquid crystals using a temperature-controlled coaxial transmission line," IEEE Trans. Microw. Theory Tech. **53**(6), 1937–1945 (2005).
19. Q. F. Liu, D. Luo, S. X. Li, and Z. Tian, "The birefringence and extinction coefficient of positive and negative liquid crystals in the terahertz range," Liq. Cryst. **43**(6), 796–802 (2016).
20. L. Yang, F. Fan, M. Chen, X. Zhang, J. Bai, and S. Chang, "Magnetically induced birefringence of randomly aligned liquid crystals in the terahertz regime under a weak magnetic field," Opt. Mater. Express **6**(9), 2803–2811 (2016).
21. R. Dickie, P. Baine, R. Cahill, E. Doumanis, G. Goussetis, S. Christie, N. Mitchell, V. Fusco, D. Linton, J. Encinar, R. Dudley, M. Naftaly, M. Arrebola, and G. Toso, "Electrical characterisation of liquid crystals at millimetre wavelengths using frequency selective surfaces," Electron. Lett. **48**(11), 611–612 (2012).
22. F. Yang and J. R. Sambles, "Determination of the microwave permittivities of nematic liquid crystals using a single-metallic slit technique," Appl. Phys. Lett. **81**(11), 2047–2049 (2002).
23. F. Y. Meng, Q. Wu, D. Erni, K. Wu, and J. C. Lee, "Polarization-Independent Metamaterial Analog of Electromagnetically Induced Transparency for a Refractive-Index-Based Sensor," IEEE Trans. Microw. Theory Tech. **60**(10), 3013–3022 (2012).
24. X. Q. Lin, Z. Chen, J. W. Yu, P. Q. Liu, P. F. Li, and Z. D. Chen, "An EIT-Based Compact Microwave Sensor With Double Sensing Functions," IEEE Sens. J. **16**(2), 293–298 (2016).
25. Z.-G. Dong, H. Liu, J.-X. Cao, T. Li, S.-M. Wang, S.-N. Zhu, and X. Zhang, "Enhanced sensing performance by the plasmonic analog of electromagnetically induced transparency in active metamaterials," Appl. Phys. Lett. **97**(11), 114101 (2010).
26. "Workflow and Solver Overview-CST Microwave Studio," CST Corp. Germany. https://www.rose-hulman.edu/class/ee/HTML/ECE340/PDFs/MWS_Tutorials.pdf.
27. N. Papasimakis, Y. H. Fu, V. A. Fedotov, S. L. Prosvirnin, D. P. Tsai, and N. I. Zheludev, "Metamaterial with polarization and direction insensitive resonant transmission response mimicking electromagnetically induced transparency," Appl. Phys. Lett. **94**(21), 211902 (2009).
28. Y. Utsumi, T. Kamei, and R. Naito, "Dielectric properties of microstrip-line adaptive liquid crystal devices," Electron. Commun. Jpn. Part II Electron. **87**(10), 13–24 (2004).
29. U. Chodorow, J. Parka, and K. Garbat, "Spectral and photorefractive properties of nematic liquid crystals from the CHBT family in the terahertz range," Liq. Cryst. **40**(8), 1089–1094 (2013).
30. L. Duvillaret, F. Garet, and J. L. Coutaz, "A reliable method for extraction of material parameters in terahertz time-domain spectroscopy," IEEE J. Quantum Electron. **2**(3), 739–746 (1996).
31. L. Zhu, J. H. Fu, F. Y. Meng, X. M. Ding, L. Dong, and Q. Wu, "Detuned magnetic dipoles induced transparency in microstrip line for sensing," IEEE Trans. Magn. **50**(1), 1–4 (2014).
32. C.-Y. Chen, I. W. Un, N. H. Tai, and T. J. Yen, "Asymmetric coupling between subradiant and superradiant plasmonic resonances and its enhanced sensing performance," Opt. Express **17**(17), 15372–15380 (2009).
33. D. E. Schaub and D. R. Oliver, "A Circular Patch Resonator for the Measurement of Microwave Permittivity of Nematic Liquid Crystal," IEEE Trans. Microw. Theory Tech. **59**(7), 1855–1862 (2011).

Optics EXPRESS

1. Introduction

Due to its tunable permittivity and relatively low dielectric loss over a wide frequency range from several gigahertzes to optical spectrum, nematic liquid crystals (NLCs) have been widely applied in reconfigurable devices, such as tunable phase shifters [1–3], reflectarrays [4–7], leaky-wave antennas [8, 9], frequency selective surfaces (FSSs) [10, 11] and liquid crystal display (LCD) screens. In fact, the loss tangent of most NLCs shows a general downward trend as frequency increases [12, 13], which is an advantage over other kinds of tunable components such as semiconductor solutions, radio frequency micro-electro-mechanical systems (MEMS) and ferroelectrics e.g. barium-strontium-titanate (BST) [14]. Moreover, NLC-based techniques features low fabrication costs, simple biasing network and ease of integration [4]. Therefore, NLC is a kind of promising material in the development of reconfigurable devices for higher frequency, especially for THz band, many investigations have been carried out. Such as the NLC-based tunable THz metamaterials [15] and the advanced modeling techniques of liquid-crystals for terahertz applications [16, 17].

In the design and optimization of NLC-based tunable devices, the characterization of NLC is essential [12, 18]. Free-space methods based on transmission-line (transmission type) or Fabry-Perot (resonant type) theorem are commonly used to extract the complex permittivity at THz band [19–21]. Directly curve fitting or a closed form relation can be applied in these methods since the **E** field is with the same direction everywhere and explicit. However, both of the transmission and resonant types are sensitive to the thickness of the NLC layer because phase information of the transmission coefficient is needed in the permittivity extraction procedure.

On the other hand, the concept of electromagnetically induced transparency (EIT) has gained a lot of attention in the free-space material characterization recently because it features sharp transmission window providing an accurate frequency response to the permittivity [23–25]. In addition, the electromagnetic (EM) field is concentrated around the metal layer making the EIT-based sensor insensitive to the thickness of material under test. However, up to now, the EIT-based sensor is only applied in the characterization of isotropic materials by directly curve-fitting [23–25] because the field distribution around the EIT structure is complicated and therefore closed form expressions between the complex permittivity and the frequency response is difficult or even impossible to derive. For the anisotropic case, situation gets more complicated and no relevant reports can be found.

In this paper, we utilize EIT structure to extract the complex permittivity of NLC, which is anisotropic. A novel algorithm is presented to extract the complex permittivity of NLCs at THz band. Firstly, the relative permittivity is extracted regardless of dielectric losses of the NLC because it has little influence on the resonant frequency of the EIT sensor. Secondly, the loss tangent is determined based on the obtained relative permittivity in the first step. Two surface fitting functions are established by changing the polarization configuration of the incident wave. A nonlinear optimization process is applied to find the minimum of the target error functions. The proposed method retains the EIT's properties of high accuracy of frequency response and high robustness to the thickness of the NLC layer, which paves the way for the anisotropic material characterization based on EIT sensor.

2. The proposed EIT based sensor

The schematic layout of the EIT based sensor, including all geometrical parameters, is shown in Fig. 1(a). The gold layer is a Jerusalem cross structure with four gaps in the four quadrants, which is deposited on a fused silica substrate and then is spin-coated with rubbed polyimide thin layer for alignment purpose [4]. The proposed EIT sensor features a 90°-rotation symmetry. Therefore, before loaded with anisotropic NLCs, its electromagnetic response is identical in both x and y directions, which is important for the following extraction procedure. To contain the NLC, another fused silica with same surface treatment

Optics EXPRESS

without metal layer is stacked on the top of the EIT sensor supported by spherical spacers forming an EIT sensor based NLC cell [refer to Fig. 1(b)].

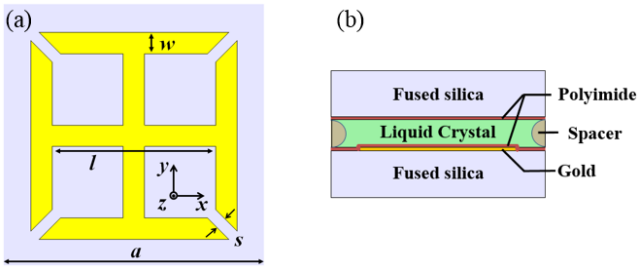

Fig. 1. Schematic layout of (a) the EIT sensor and (b) the EIT sensor based NLC cell.

The schematic layout of the EIT based sensor, including all geometrical parameters, is shown in Fig. 1(a). The gold layer is a Jerusalem cross structure with four gaps in the four quadrants, which is deposited on a fused silica substrate and then is spin-coated with rubbed polyimide thin layer for alignment purpose [4]. The proposed EIT sensor features a 90°-rotation symmetry. Therefore, before loaded with anisotropic NLCs, its electromagnetic response is identical in both x and y directions, which is important for the following extraction procedure. To contain the NLC, another fused silica with same surface treatment without metal layer is stacked on the top of the EIT sensor supported by spherical spacers forming an EIT sensor based NLC cell [refer to Fig. 1(b)].

Numerical simulation of the proposed EIT based NLC cell is performed by the frequency domain solver in CST Microwave Studio (MWS) [26] to demonstrate the EIT effect. The geometry of the unit cell is designed as w = 55 μm, l = 420 μm, a = 700 μm and s = 30 μm. The thickness of the NLC layer is 120 μm. The fused silica has a permittivity of 3.78, a loss tangent of 0.0015, and a thickness of 300 μm. Boundary condition of "unit cell" is applied in x and y direction and a Gaussian pulse with a spectrum ranging from 250 GHz to 350 GHz is chosen as the excitation signal. The dielectric constants $\varepsilon_{r\perp}$ and $\varepsilon_{r\parallel}$ of NLC is assumed as 2 and 4, respectively, regardless of dielectric losses for time-saving purpose. $\mu_r = 1$ is always valid for NLCs as it is a non-ferromagnetism material [18]. The polarization of the normally incident plane wave and the orientation of NLC molecules $\vec{n}$ are in the same direction along y-axis. The corresponding transmission coefficient of the sensor is depicted in Fig. 2. a sharp transmission peak (i.e. a transparent window) can be observed between two stop-bands, which can be regarded as the EIT-like effect brought by the excitation of the trapped mode, a high-Q mode formed by counter-propagating currents [27]. The sharp resonant of the EIT sensor provides an accurate strategy for the characterization of NLCs.

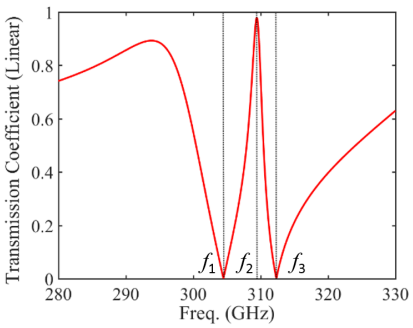

Fig. 2. Transmission coefficient of the sensor.

Optics EXPRESS

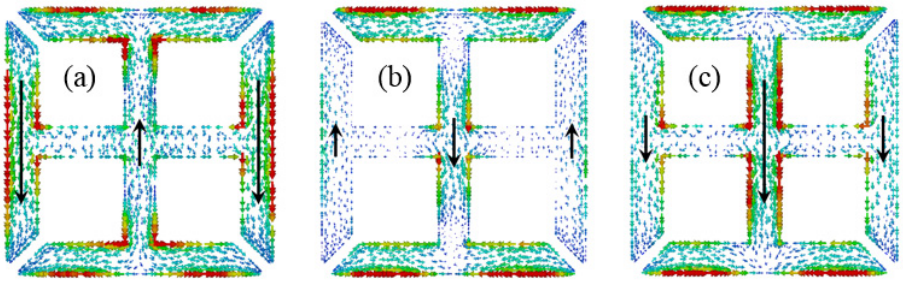

Fig. 3. Current distributions of the EIT sensor at (a) f_1 = 304.50 GHz, (b) f_2 = 309.46 GHz and (c) f_3 = 312.35 GHz, respectively.

To visualize the physical mechanism of the transparency window, the current distributions induced by the incident plane wave at f_1 = 304.50 GHz, f_2 = 309.46 GHz and f_3 = 312.35 GHz, respectively, are simulated and compared as shown in Fig. 3. Remarkable resonances of dipole mode [27] can be observed in Figs. 3(a) and 3(c) (i.e. current oscillations symmetric with respect to *y*-axis in outer and inner strips, respectively). The re-radiated electric field by the resonant strip(s) is considerably enhanced and has opposite phase with respect to the incident electric field, which leads to the two stop-bands in the transmission spectrum of Fig. 2. In Fig. 3(b), the induced currents of the inner and outer strips appear to be similar magnitude with opposite phase. The re-radiated electric field is very weak and hence has little influence on the incident electric field. The transparent window is therefore formed.

3. Extraction of complex permittivity

3.1 Theory description

There are four parameters: $\varepsilon_{r\perp}$, $\varepsilon_{r\|}$, $\tan\delta_\perp$ and $\tan\delta_\|$ to be estimated in the characterization of NLCs. In conventional technique of the free-space permittivity extraction of NLCs, electric field **E** in the NLC layer is with the same direction everywhere, such as parallel slabs based transmission type [19, 20] and Fabry-Perot cavity based resonant type [21, 22] structures. Therefore, the parallel components: $\varepsilon_{r\|}$, $\tan\delta_\|$ and the vertical components: $\varepsilon_{r\perp}$, $\tan\delta_\perp$ can be independently derived by setting the incident electric field **E** parallel [refer to the case 1 shown in Fig. 4(a)] and perpendicular [refer to Fig. 4(b), namely, case 2] to the orientation of NLC molecules $\vec{n}$, respectively. However, the distribution of electric field **E** is complicated and multi-directional in the NLC region for the proposed EIT sensor as depicted in Fig. 4(c). The transmission coefficients of case 1 and case 2 are no longer independently determined by parallel and vertical components of the NLC. In other words, the existing algorithm is invalid for the EIT-based permittivity extraction of NLCs.

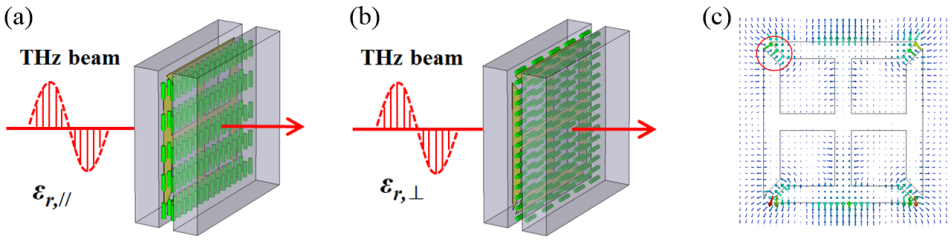

Fig. 4. Schematics of the two configurations with the orientation of the NLC molecules parallel (a) and perpendicular (b) to the incident (**E**) field denoted as Case 1 (extraordinary transmission) and Case 2 (ordinary transmission), respectively. The two cases can be switched by rotating the sample with 90 degree; (c) (**E**)-field distribution in the NLC layer.

Optics EXPRESS

The NLC is low-loss medium with the typical loss tangent in the order of 10^{-2}. The influence of tanδ on the frequency shift can be therefore neglected [28]. For further explanation, two types of NLCs with different loss-tangent combinations are filled into the EIT cell. Simulation results are shown in Fig. 5. The variation of tan$\delta_{\|,\perp}$ has little influence on the resonant frequency in both cases, which means that the resonant frequency of the EIT-based sensor is approximately determined by the real part of the complex permittivity. In addition, the distribution of electric field **E** is also primarily sensitive to the $\varepsilon_{r\|}$, $\varepsilon_{r\perp}$, which is closely related to the power dissipation level of the sensor. Therefore, the extraction of the dielectric properties of the NLCs is performed by two separate steps. Firstly, extract the $\varepsilon_{r\|}$, $\varepsilon_{r\perp}$ from the resonant frequencies. Then determine the tan$\delta_{\|}$, tan$\delta_{\perp}$ from the quality factor Q based on the extracted $\varepsilon_{r\|}$, $\varepsilon_{r\perp}$.

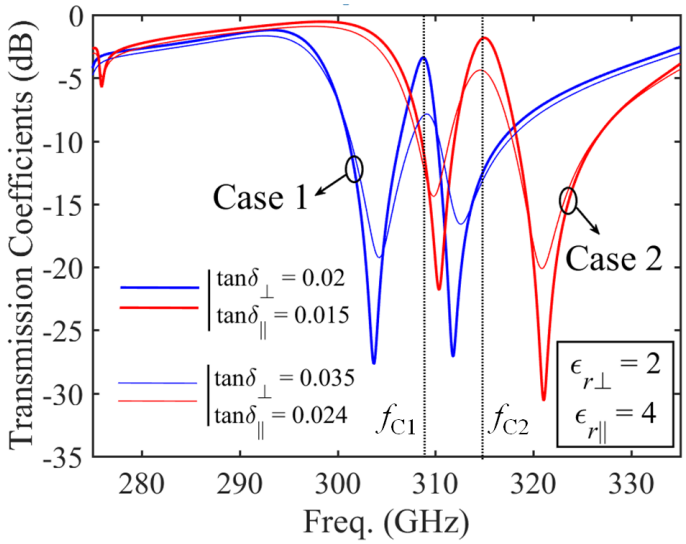

Fig. 5. Frequency response to the NLCs with the identical relative permittivity ($\varepsilon_{r\perp} = 2$, $\varepsilon_{r\|} = 4$) and different loss-tangent combinations (tan$\delta_{\|} = 0.015$, tan$\delta_{\perp} = 0.02$ and tan$\delta_{\|} = 0.024$, tan$\delta_{\perp} = 0.035$) in Case 1 and Case 2.

3.2 Relative permittivity extraction

Due to the complicated field distribution in the EIT sensor, closed form expression of the relation between the relative permittivity $\varepsilon_{r\|}$, $\varepsilon_{r\perp}$ and the corresponding resonant frequency f_{C1}, f_{C2} (resonant frequency in Case 1 and Case 2) is difficult or even impossible to derive. It is worth noting that in the millimeter and sub-millimeter wave band, according to [10, 12, 19–22, 29], the relative permittivity of NLCs satisfies the follow relation without exception as

$$2<\varepsilon_{r\perp}<\varepsilon_{r\|}<4. \tag{1}$$

In this case, numerical simulations are carried out by calculating each point in the permittivity plane [$\varepsilon_{r\|}$(2:4), $\varepsilon_{r\perp}$(2:4)] with a fixed step length of 0.01. Configurations of the simulation model are shown in Fig. 4 (a) and (b). The results of f_{C1}, f_{C2} versus $\varepsilon_{r\|}$, $\varepsilon_{r\perp}$ are plotted in Fig. 6.

Optics EXPRESS

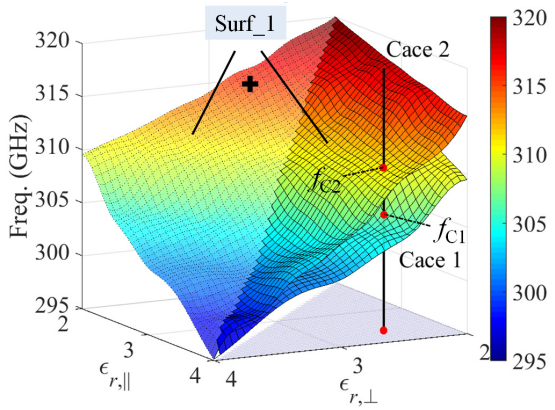

Fig. 6. Numerical results of resonant frequencies f_{C1}, f_{C2} versus relative permittivities $\varepsilon_{r\|}$, $\varepsilon_{r\perp}$.

It is obvious that the resonant frequency decreases with the $\varepsilon_{r\|}$, $\varepsilon_{r\perp}$ in both cases. The three points f_{C1}, f_{C2} and the corresponding ($\varepsilon_{r\|}$, $\varepsilon_{r\perp}$) are collinear and parallel to z-axial [red dots in Fig. 6]. f_{C1} is equal to f_{C2} at the points meeting $\varepsilon_{r\|} = \varepsilon_{r\perp}$ (isotropic case). Referring to the diagram, the $\varepsilon_{r\|}$ and $\varepsilon_{r\perp}$ can be extracted according to the obtained f_{C1} and f_{C2}. However, in practice, directly checking diagram is not an artful method for the parameters extraction. In order to conduct the extraction procedure automatically through using computers, the plotted surfaces for the Cases 1 and 2 can be fitted by two polynomial functions. Since a full surface, namely, Surf_1 [refer to Fig. 6] can be modeled by mirroring the surface of Case 1 from variable area of $\varepsilon_{r\|} > \varepsilon_{r\perp}$ to $\varepsilon_{r\|} < \varepsilon_{r\perp}$ along the diagonal line $\varepsilon_{r\|} = \varepsilon_{r\perp}$, the two fitting functions will therefore feature identical polynomial coefficient P_{mn} (listed in Table 1) with transposed $\varepsilon_{r\|}$ and $\varepsilon_{r\perp}$ as

$$f_{C1}\left(\vec{\varepsilon}_r\right) = \sum_{m=0}^{m=3}\sum_{n=0}^{n=5} P_{mn}\varepsilon_{r\|}^{m}\varepsilon_{r\perp}^{n} \tag{2}$$

$$f_{C2}\left(\vec{\varepsilon}_r\right) = \sum_{m=0}^{m=3}\sum_{n=0}^{n=5} P_{mn}\varepsilon_{r\perp}^{m}\varepsilon_{r\|}^{n} \tag{3}$$

where

$$\vec{\varepsilon}_r = \begin{pmatrix} \varepsilon_{r\|} \\ \varepsilon_{r\perp} \end{pmatrix} \tag{4}$$

defines a position in the plane ($\varepsilon_{r\|}$, $\varepsilon_{r\perp}$). The chosen order of the polynomial is 3, 5 with a root-mean-square error (RMSE) of 0.42 GHz because no remarkable improvements of fitting level can be achieved for higher order indexes. Deviations in the extracted permittivity brought by this discrepancy will be discussed in following segment.

Table 1. Polynomial Coefficients of the Fitting Function

P_{mn}	0	1	2	3	4	5
0	1631	–1309	517	–114.2	15.92	–1.059
1	–989.7	781.9	–187.2	13.12	–0.073	0
2	300.9	–218.2	43.28	–1.743	0	0
3	–31	20.8	–3.32	0	0	0

The next step is to search for the zeros of f_{C1} - f_{C1m}, and f_{C2} - f_{C2m} simultaneously, where f_{C1m} and f_{C2m} are the measured resonant frequencies in Case 1 and Case 2, respectively. Due to the nonlinearity of these Eqs, numerical solution is necessary. One of the methods to solve

such a root finding problem is the Newton-Raphson iteration. However, this method is applicable only if the initial values of $\varepsilon_{r\parallel}$ and $\varepsilon_{r\perp}$ are very closed to the final solution, otherwise it could be diverged [30]. In this case, we use the nonlinear optimization method to search the minimum of the error function as

$$\delta(\vec{\varepsilon}_r)=\delta_{C1}^2+\delta_{C2}^2 \tag{5}$$

where

$$\delta_{C1}\left(\vec{\varepsilon}_r\right)=f_{C1}\left(\vec{\varepsilon}_r\right)-f_{C1m} \tag{6}$$

and

$$\delta_{C2}\left(\vec{\varepsilon}_r\right)=f_{C2}\left(\vec{\varepsilon}_r\right)-f_{C2m}. \tag{7}$$

This error function is similar to a paraboloid as shown in Fig. 7, which is quite simple and low dimension. Therefore, the calculation of the inverse Hessian matrix $H_\delta^{-1}\left(\vec{\varepsilon}_r^{(k)}\right)$ of the error function can be made directly without requiring complex procedures [30]. Then the solution can be obtained by the iteration procedure as

$$\vec{\varepsilon}_r^{(k+1)}=\vec{\varepsilon}_r^{(k)}-H_\delta^{-1}\left(\vec{\varepsilon}_r^{(k)}\right)\cdot\vec{\nabla}\delta\left(\vec{\varepsilon}_r^{(k)}\right) \tag{8}$$

where the subscript k is the number of iteration steps. Assuming the case of f_{C1m} = 306.1 GHz, f_{C2m} = 310.3 GHz (corresponding to $\varepsilon_{r\perp}$ = 2.5, $\varepsilon_{r\parallel}$ = 3.3 in the simulation results), the solution of the proposed extraction method converges to the point $\varepsilon_{r\perp}$ = 2.48, $\varepsilon_{r\parallel}$ = 3.27 as depicted in the inset of Fig. 7.

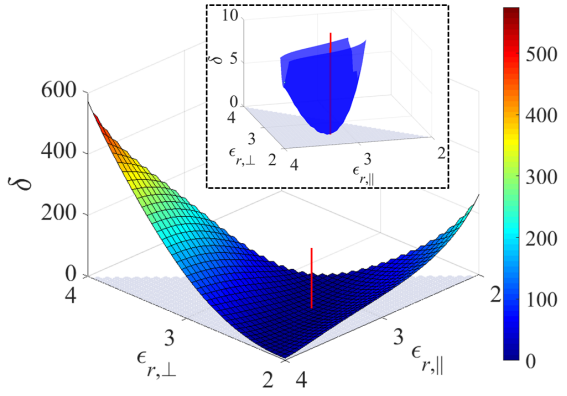

Fig. 7. Error function δ versus $\varepsilon_{r\parallel}$, $\varepsilon_{r\perp}$ with assumption: f_{C1m} = 306.1 GHz and f_{C2m} = 310.3 GHz.

The relative permeability of NLC is μ_r = 1. Then the sensitivity m_{NLC} [the resonance wavelength shift over the refractive index change unit (RIU)] of the EIT sensor can be defined and calculated as

$$m_{NLC}=\frac{\lambda_{C1}-\lambda_{C2}}{\sqrt{\varepsilon_{r\parallel}}-\sqrt{\varepsilon_{r\perp}}}=56.8\ \text{m/RIU} \tag{9}$$

Optics EXPRESS

where λ_{C1}, λ_{C2} is the resonant wavelength of Case 1 and Case 2, respectively. This definition is different from that proposed in [24], which is only suitable for the isotropic rather than anisotropic case. The average FWHM (Full Width Half Maximum) of the sensor in the two cases is 8.21 μm. Then the Figure of Merit (FoM) is defined and calculated as

$$\mathrm{FoM} = \frac{m_{\mathrm{LC}}(\ \mathrm{m/RIU})}{\mathrm{FWHM}} = 6.92. \tag{10}$$

We have compared the corresponding FoM values of sensing refractive index (permittivity) based on EIT-like sensor with coupled split-ring and spiral structure [23], Jerusalem cross in ring type [24], detuned split ring [31], planar EIT-like metamaterial [32], and our proposed EIT-like sensor. The sensing performance of our EIT-like sensor is comparable with other works as listed in Table 2. It is worth noting that only this work is applicable for the characterization of anisotropic material whereas the others are for the isotropic case.

Table 2. Comparison Between FoM Values of Different Methods

Material Under Test	Isotropic				Anistropic
Method	[23]	[24]	[31]	[32]	This work
FoM	8.14	11.9	6.17	7.4	6.92

3.3 Loss tangent extraction

Once the relative permittivity is obtained, we can extract the loss tangent tan$\delta_{\|}$, tan$\delta_{\perp}$ of the NLC using same procedure aforementioned. Firstly, numerical simulations are carried out and the results of Q_{C1}, Q_{C2} versus tan$\delta_{\|}$, tan$\delta_{\perp}$ in both cases are plotted in Fig. 8.

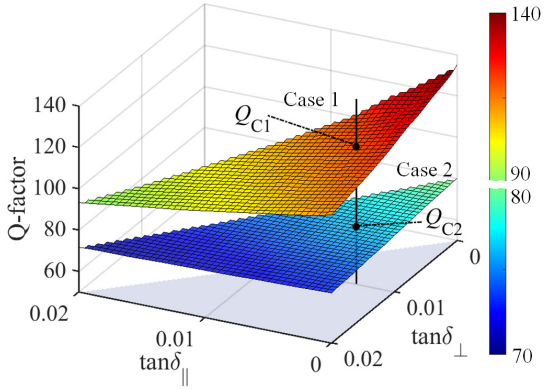

Fig. 8. Numerical results of quality factors Q_{C1}, Q_{C2} versus loss tangents tan$\delta_{\|}$, tan$\delta_{\perp}$ under the condition of $\varepsilon_{r\perp} = 2.48$, $\varepsilon_{r\|} = 3.27$.

The half-power frequencies f_1 and f_2 are used to determine the resonant frequency

$$f_0 = \sqrt{f_1 f_2} \tag{11}$$

and the quality factor is defined as

$$Q = \frac{f_0}{f_2 - f_1} \tag{12}$$

Using (11) instead of the absolute peak in transmission magnitude provides a more accurate estimate of the center frequency in the presence of noise [33].

The different field distribution of two cases making the Q-factors in different level, which are not continuous at tan$\delta_{\|}$ = tan$\delta_{\perp}$. Therefore, the polynomial coefficients of the fitting

Optics EXPRESS

functions are different in the two cases, which is denoted as P_{mn}^{C1} and P_{mn}^{C2}, respectively. The polynomial functions are established as

$$Q_{C1}\left(\vec{\alpha}\right)=\sum_{m=0}^{m=3}\sum_{n=0}^{n=3}P_{mn}^{C1}\tan^{m}\delta_{\parallel}\tan^{n}\delta_{\perp} \tag{13}$$

$$Q_{C2}\left(\vec{\alpha}\right)=\sum_{m=0}^{m=3}\sum_{n=0}^{n=3}P_{mn}^{C2}\tan^{m}\delta_{\parallel}\tan^{n}\delta_{\perp} \tag{14}$$

where

$$\vec{\alpha}=\begin{pmatrix}\tan\delta_{\parallel}\\ \tan\delta_{\perp}\end{pmatrix} \tag{15}$$

defines a position in the plane ($\tan\delta_{\parallel}$, $\tan\delta_{\perp}$). The chosen order of the polynomial is 3, 3 with a RMSE of 0.13. Deviations in the extracted loss tangent brought by this discrepancy will also be discussed in following segment. Then the error function is defined as

$$\delta(\vec{\alpha})=\delta_{C1}^{2}+\delta_{C2}^{2} \tag{16}$$

where

$$\delta_{C1}\left(\vec{\alpha}\right)=\ln\left(Q_{C1}\left(\vec{\alpha}\right)\right)-\ln\left(Q_{C1m}\right) \tag{17}$$

and

$$\delta_{C2}\left(\vec{\alpha}\right)=\ln\left(Q_{C2}\left(\vec{\alpha}\right)\right)-\ln\left(Q_{C2m}\right). \tag{18}$$

This error function is also similar to a paraboloid as shown in Fig. 9 and similar iteration procedure is carried out as

$$\vec{\alpha}^{(k+1)}=\vec{\alpha}^{(k)}-H_{\delta}^{-1}\left(\vec{\alpha}^{(k)}\right)\cdot\vec{\nabla}\delta\left(\vec{\alpha}^{(k)}\right). \tag{19}$$

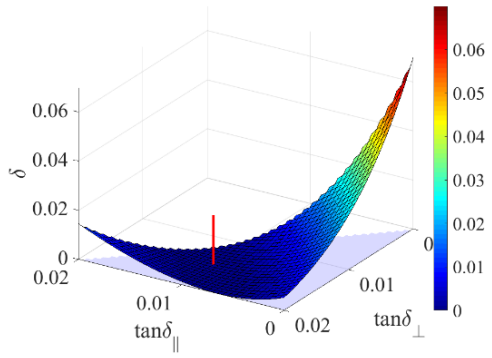

Fig. 9. Error function δ versus $\tan\delta_{\parallel}$, $\tan\delta_{\perp}$ under the condition of Q_{C1m} = 104.72, Q_{C2m} = 74.21, f_{C1m} = 306.1 GHz and f_{C2m} = 310.3 GHz.

As depicted in the inset Fig. 10, the solution is $\tan\delta_{\parallel}$ = 0.01, $\tan\delta_{\perp}$ = 0.0147 assuming the case of Q_{C1m} = 104.72, Q_{C2m} = 74.21 and f_{C1m} = 306.1 GHz and f_{C2m} = 310.3 GHz.

Optics EXPRESS

3.4 Uncertainty analysis

The inherent uncertainty in the extracted complex permittivity is caused by the discrepancies between the fitting function and the numerical data. The maximum root-mean-square error (RMSE) of the Eqs. (4) and (5) is 0.42 GHz. To evaluate the uncertainty of the calculated relative permittivity brought by this frequency discrepancy, all of eight frequency combinations are considered with a variation step of 0.42 GHz, which is denoted as ($f_{C1} \pm 0.42, f_{C2}$), ($f_{C1}, f_{C2} \pm 0.42$), ($f_{C1} \pm 0.42, f_{C2} \pm 0.42$).

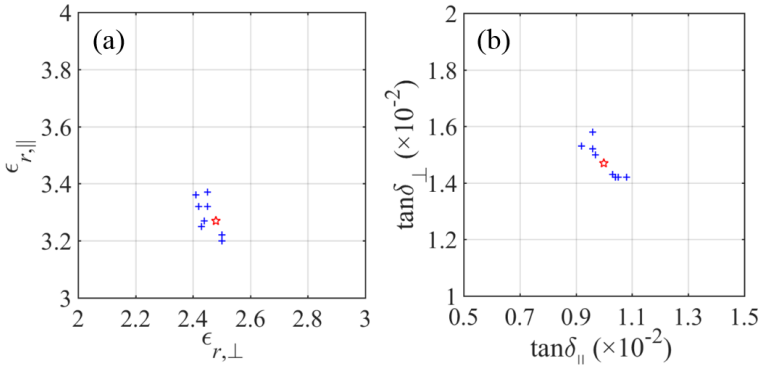

Fig. 10. Deviations in the relative permittivity (a) and loss tangent (b) brought by the inherent error of the proposed technique (the results with and without deviations are marked as stars and crosses, respectively).

The corresponding results of the relative permittivity are calculated and shown in Fig. 10(a) indicating that the uncertainty of $\varepsilon_{r\parallel}$ and $\varepsilon_{r\perp}$ is 3% and 2.8%, respectively. As the maximum RMSE of the Eqs. (15) and (16) is 0.13, same procedure is applied to determine the uncertainty of the loss tangent. The results calculated from eight Q-factor combinations ($Q_{C1} \pm 0.13$, Q_{C2}), (Q_{C1}, $Q_{C2} \pm 0.13$), ($Q_{C1} \pm 0.13$, $Q_{C2} \pm 0.13$) are shown in Fig. 10(b). The uncertainty of tan$\delta_\perp$ and tan$\delta_\parallel$ is 7.6% and 8.2%, respectively.

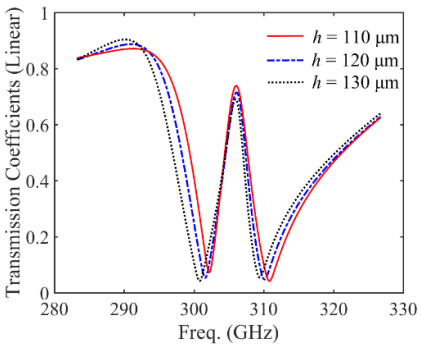

Fig. 11. Transmission coefficients of the proposed EIT sensor with different thickness of the NLC layer.

Additional error is originated from the fabrication tolerance. In fact, the discrepancies of geometry dimensions can be neglected for the existing fabrication technology. For instance, with the typical dimensional tolerance of 2-μm [5], the shift of resonant frequency of numerical results is less than 0.17 GHz. To determine the uncertainty in the frequency deviation to the thickness variation of the NLC layer, a numerical sensitivity analysis is applied as shown in Fig. 11. The shift of resonant frequency is less than 0.1 GHz with the thickness variation from 110 μm to 130 μm implying the high robustness of the proposed method compared to the conventional design.

Optics EXPRESS

4. Conclusion

For the first time we introduce the concept of electromagnetically induced transparency (EIT) into the permittivity extraction of the anisotropic material (NLCs). Firstly, An EIT sensor featuring sharp transmission peak with 90°-rotation symmetry is designed to make it polarization independent in x and y direction. Secondly, a two-step extraction strategy is proposed by extracting the relative permittivity and the loss tangent from the resonant frequencies and the quality factor Q, respectively. A nonlinear optimization process is applied to find the minimum of the target error functions. Finally, uncertainty analysis is carried out to evaluate the permittivity deviation brought by the inherent error of the technique. The proposed method retains the EIT's properties of high accuracy of frequency response and high robustness to the thickness of the NLC layer, which paves the way for the anisotropic material characterization based on EIT sensor.

Funding

National Natural Science Foundation of China (NSFC) (61671180, 61501275); Science Foundation Project of Heilongjiang Province of China (QC2015073); Deutsche Forschungsgemeinschaft (DFG) in the framework of DFG SFB/TRR 196 MARIE under Project S03.